Catalysis Letters 57 (1999) 81–88



# Influence of the nanostructure and morphology of $(VO)_2P_2O_7$ on its catalytic reactivity

N. Duvauchelle and E. Bordes *

*Département de Génie Chimique, Université de Technologie de Compiègne, BP 20529, F-60205 Compiègne Cedex, France*
E-mail: elisabeth.bordes@utc.fr; elisabeth.bordes@univ-lille1.fr

Received 10 June 1998; accepted 7 December 1998

The reoxidability of vanadyl pyrophosphate is studied by thermal analysis and by temporal analysis of product (TAP). The samples differ by surface area, oxidation state of vanadium, crystallite size, and degree of crystallinity. The morphology ranges from platy to prismatic and the microstructure from mosaic crystals exhibiting {100} faces to bulky crystals. The reactivity of these samples during oxidation as well as their catalytic reactivity studied in flow reactor is accounted for by the microstructure. The highest reoxidation capability and the best catalytic properties in oxidation of $n$-butane to maleic anhydride are obtained with mosaic crystals.

**Keywords:** mosaic crystals, nanostructure, vanadyl pyrophosphate, oxygen capacity, $n$-butane oxidation

## 1. Introduction

The catalytic performance is a complex interplay of various but interdependent properties of the solid [1,2]. In selective oxidation reactions, both steps of activation of the hydrocarbon (activity) and of oxygen insertion (selectivity) depend on the amount and on the "quality" of the lattice surface oxygens. Obviously, these steps also depend on the valence state of the cations.

The oxidizing character of the catalytic solid deals not only with thermodynamics (redox couple), but also with kinetics since the mobility of the surface oxygens is involved. To close the catalytic cycle, the vacancies created by the reactant are refilled by gaseous and/or bulk oxygen, depending on the relative contribution of each process. An ideal catalyst would work only by its surface, but actually it does not. Once the microstructure exhibited by the surface has been determined by the operating conditions during synthesis and calcination, the reactivity of the bulk is still involved for the whole catalyst life. Indeed, during the catalytic steps of activation, equilibration, reaction, ageing, the diffusion of vacancies to the bulk and of oxygens to the surface modifies the bulk more or less strongly, and consequently it affects the surface properties at a nanoscale. The reduction of oxide catalysts has been the matter of numerous studies. For example, in V, Mo and W oxides of $ReO_3$ type, crystallographic shear planes have been evidenced by electron microscopy [3,4] and more recently by STM and AFM [5,6]. Now Gai [7] assumes that gliding planes are acting during catalytic reaction, mostly in the case of $(VO)_2P_2O_7$. The reoxidability of the catalyst is also a very important parameter, but it is less easy to study from a mechanistic point of view. The case of vanadyl pyrophosphate, generally considered as the active and selective phase for the mild oxidation of $n$-butane to maleic anhydride [8], is worthwile to consider because the rate-limiting step is the reoxidation, contrary to most oxides.

In the composition range $P/V = 0.9$–$1.2$ of catalysts, vanadyl pyrophosphate is detected by X-ray diffraction (XRD), but its microstructure depends strongly on the way it has been prepared [9]. The state of $(VO)_2P_2O_7$ ranges from amorphous to crystallized depending on several factors that will not be detailed here. In a recent study [10], we have shown that the pseudomorphic transformation of the $VOHPO_4{\cdot}0.5H_2O$ precursor to $(VO)_2P_2O_7$ catalyst proceeds by an oriented nucleation and growth mechanism. Such a mechanism explains how the dehydration of the precursor yields particles of $(VO)_2P_2O_7$ which are constituted by a great number of monocrystalline, slightly misoriented, nanocrystallites. As noted previously by Torardi et al. [11], the creation of additional basal surface area during the breaking up of the single-crystal precursor into many small crystals of pyrophosphate may be beneficial for catalytic performance. However, no study addresses the role of this particular nanostructure on the catalyst reactivity, and particularly on the reoxidation step. The latter is as important as it is the rate-limiting step in the mechanism of Mars and van Krevelen [12], and as it depends on the operating conditions prevailing in the reactor [13]. In this paper, the reoxidability of the catalyst, studied by TGA and by a transient vacuum method (TAP), is related to its microstructure and morphology. Since the (catalytic or non-catalytic) reactivity depends on the crystal morphology, we have used well-defined samples of $(VO)_2P_2O_7$ already characterized in a previous work [10] to examine their catalytic properties.

* To whom correspondence should be addressed.

Table 1
Characteristics of $(VO)_2P_2O_7$ samples prepared at various temperatures and times of calcination.

| | Temperature of calcination (°C) | Time of calcination (h) | Color | Surface area ($m^2/g$) | Oxidation state of vanadium[a] | Average crystallite size[b] $L_m$ (Å) | Internal strain[b] $\beta$ ($\times 10^{-3}$) |
|---|---|---|---|---|---|---|---|
| Pyro-420 | 420 | 48 | Brown | 5.6 | 4.146 | 437 | 9.26 |
| Pyro-750 | 750 | 3 | Grey | 6.1 | 4.012 | 995 | 6.53 |
| Pyro-870 | 870 | 24 | Blue-grey | 1 | –[c] | $\gg$1000 | 4.32 |

[a] Potentiometric titration [13].
[b] Calculated by the method of Williamson and Hall [12].
[c] Titration could not be made because of non-dissolution of the sample.

## 2. Experimental

### 2.1. Preparation

The precursor $VOHPO_4 \cdot 0.5H_2O$ was prepared by refluxing a $P/V = 1:1$ mixture of $V_2O_5$ and $H_3PO_4$ (85%) during 6 h in 2-butanol. The precipitate was thoroughly washed several times with 2-butanol and acetone to remove organic residue from the solid. The resulting light green solid was dried in an oven at 120 °C (15 h). The topotactic conversion of precursor to model $(VO)_2P_2O_7$ catalyst was carried out in a tubular furnace under controlled flow of nitrogen (1 l $h^{-1}$, $P = 1$ atm, $p_{O_2} = 10^{-5}$ atm), and the solid was maintained several hours at constant temperature. Three samples of vanadyl pyrophosphate, called Pyro-420, Pyro-750 and Pyro-870, were obtained after calcination at 420, 750 and 870 °C during 48, 3 and 24 h, respectively.

### 2.2. Characterization

The vanadyl pyrophosphate samples were characterized by several methods.

XRD was performed on powders using an INEL CPS 120 (curve detector) and Cu K$\alpha_1$ radiation (0.15406 nm). The average crystallite size ($L_m$) and internal strain ($\varepsilon$) data gathered in table 1 were evaluated satisfactorily using the Williamson–Hall method [10,14].

TEM observations were made in a Jeol 1200EX microscope, operating at 80 kV to avoid modification of the sample under the beam. SEM analysis was carried out using a Jeol 840C microscope.

Fourier-transformed infrared spectra (FTIR) of powder samples pressed as KBr discs were recorded using a Perking–Elmer 1600 spectrometer in the 3600–400 $cm^{-1}$ range.

Potentiometric titration was carried out using the method of Niwa and Murakami [15] to estimate the average oxidation number of vanadium.

The specific surface area was estimated by the one-point BET method, using nitrogen gas at 77 K in a Quantasorb equipment.

### 2.3. Reactivity experiments

The oxidation of the three $(VO)_2P_2O_7$ samples has been examined by TGA in pure oxygen flow (Setaram microbalance TG 92, $p_{O_2} = 1$ atm, flow rate = 1 l $h^{-1}$). 20 mg of sample were heated up to 800 °C (heating rate 5 °C/min) and quenched at room temperature. The final product was analyzed by XRD.

Vacuum transient experiments were performed in the temporal analysis of product (TAP) reactor [16] to determine the oxygen uptake of the catalysts under the following conditions: 0.125 g of sample were loaded into the reactor between two layers of quartz powder. A $^{16}O_2$/Ne mixture (1 : 3) was pulsed at $T = 390$ °C over the catalysts and the responses to the inlet pulses were analyzed using a quadrupole mass spectrometer. The oxygen uptake was quantified using Ne as an internal standard.

The catalytic experiments were performed at 1 atm pressure in a conventional flow fixed-bed microreactor with online analysis of feed and products by gas chromatography. The stainless steel reactor containing 5 $cm^3$ of catalyst powder and 5 $cm^3$ of glass beads was heated by means of an electric furnace regulated to $\pm 1$ °C. The effluent leaving the reactor was directed to two chromatographs (FID and TCD for hydrocarbons and permanent gases, respectively). The operating conditions were 420 °C, contact time 1.5 s, feed $C_4H_{10}/O_2/N_2 = 1.5/19.7/78.8$. Blank runs showed no activity of the empty reactor. After a stabilization period, the catalytic results were stable for at least 48 h.

## 3. Results

### 3.1. $(VO)_2P_2O_7$ characterization

The physicochemical properties of the $(VO)_2P_2O_7$ samples were detailed in a previous paper [10]. The three samples differ by their color, surface area, mean oxidation state of vanadium, average crystallite size ($L_m$), degree of crystallinity ($\varepsilon$) and morphology (table 1). To summarize, the bitrapezoidal platelets of Pyro-420 lie on the (100) plane. These platelets are monocrystalline mosaic particles, i.e., they are built up by a great number of small crystallites ($L_m = 437$ Å), which are slightly misoriented with respect to each other (figure 1(A)) as accounted for by the relatively strong internal strain ($\varepsilon = 9.2 \times 10^{-3}$). The mosaic microstructure supposes that disorganized areas, consisting mainly of dislocations, separate the crystallites from each other.

This model is not well adapted to describe the bitrapezoidal platelets of Pyro-750, because they exhibit a more disturbed texture (voids, cracks, large crystallites, mosaic

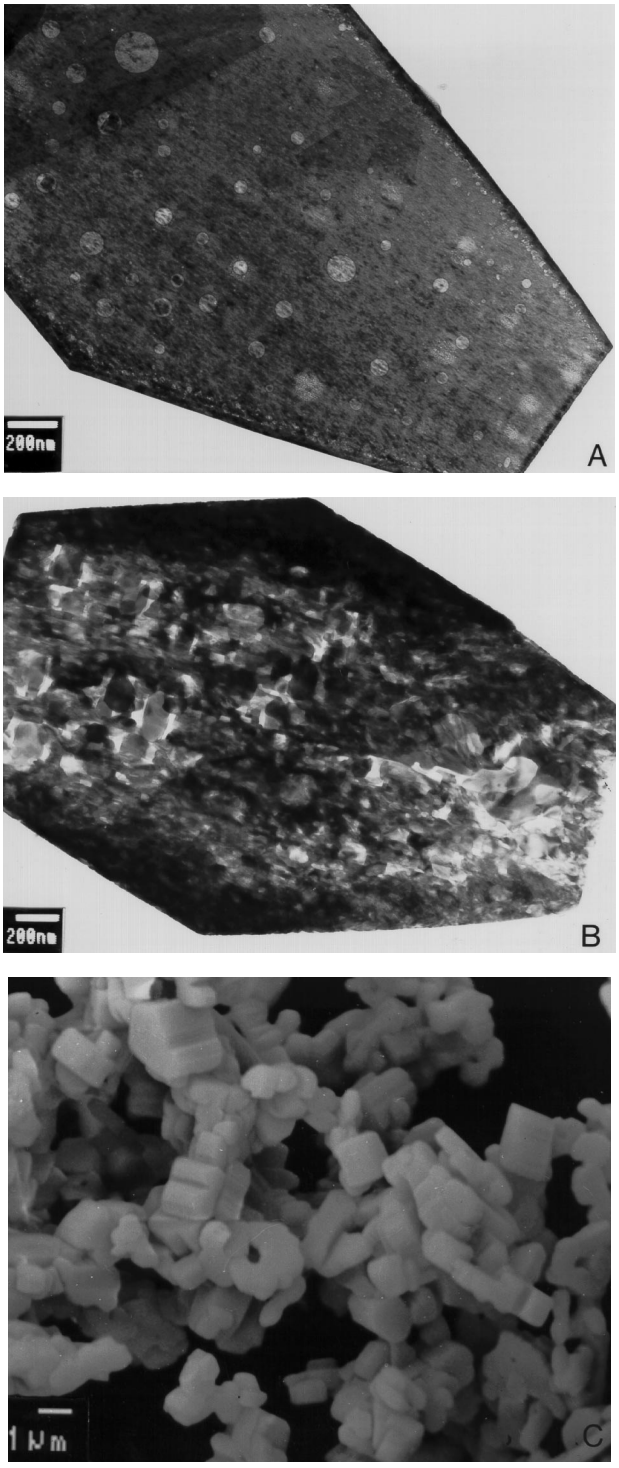


Figure 1. (A) TEM bright field image of a Pyro-420 particle. (B) TEM bright field image of a Pyro-750 particle. (C) SEM image of Pyro-870.

areas, etc.) (figure 1(B)), which results from the rearrangement of the initial mosaic microstructure during the higher-temperature process (as a whole, $L_m$ increases and $\varepsilon$ decreases) [10]. When the temperature of calcination increases up to 870°C, the crystallites that were observed for Pyro-750 are first broken and then sintered. The resulting crystalline material, Pyro-870, cannot retain the platy

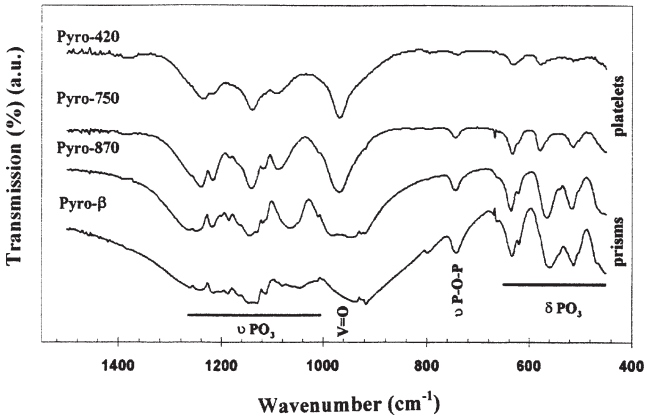


Figure 2. FT-IR spectra of $(VO)_2P_2O_7$ samples and assignment of the bands (see table 2). Pyro-$\beta$ was obtained by reduction of $\beta$-$VOPO_4$ in $N_2$ (see text).

morphology anymore. It exhibits a prismatic shape (figure 1(C)), in accordance with the equilibrium shape of $(VO)_2P_2O_7$ calculated by the Curie–Wulff method [17,18]. Therefore, the contribution of $\{100\}$ faces to the total crystal area is obviously lower than in the case of Pyro-420 and Pyro-750 bitrapezoidal platelets.

### 3.2. Infrared spectroscopy

The FT-IR powder spectra of platy (Pyro-420 and Pyro-750) and prismatic (Pyro-870) samples (figure 2) differ by the number and wavenumber of the main bands assigned to the vibrations of the $PO_3$ group and of P–O–P in $P_2O_7$, and of the vanadyl bond (table 2). Prismatic Pyro-$\beta$, obtained by calcination of $\beta$-$VOPO_4$ in $N_2$ at 760 °C (10 h) [1], exhibits the same infrared spectrum as Pyro-870. The symmetric stretching of P–O–P which occurs at 744 $cm^{-1}$ in bent pyrophosphate groups is the only one which is not modified. The spectrum of platy Pyro-750 is better resolved than that of the poorly crystallized Pyro-420 sample. More numerous bands are observed in the spectrum of Pyro-870 and Pyro-$\beta$, as if some bands of Pyro-750 were shifted and/or splitted. From Pyro-420 to Pyro-$\beta$, the bands at ca. 1237–1265 and 1139–1150 $cm^{-1}$ ($\nu_{as}$ $PO_3$) are shifted toward higher wavenumbers, while those assigned to $\nu_s$ $PO_3$ (1092–1066) are shifted to lower wavenumbers. The band at ca. 965–980 $cm^{-1}$ is generally assigned to the stretching of V=O. However, it should decrease with the valence of vanadium, and be lower for Pyro-870 than for Pyro-420 (see table 1). Because of bands assigned to $\nu_{as}$ of P–O–P for Pyro-870 and Pyro-$\beta$ (which are absent for platy samples) it is difficult to be sure that this assignment is right.

These two kinds of spectra were already observed for samples obtained by calcination in nitrogen of plates of $VOHPO_4{\cdot}0.5H_2O$ or of $\gamma$-$VOPO_4$, and of $\beta$-$VOPO_4$, respectively [19,20]. At that time, we thought that two polymorphs of $(VO)_2P_2O_7$, called "$\gamma$" and "$\beta$", respectively, could exist, because they give back $\gamma$-$VOPO_4$ and $\beta$-$VOPO_4$, respectively, by reoxidation. Experiments to ev-

Table 2
Infrared absorption bands of Pyro-420, Pyro-750, Pyro-870 and Pyro-$\beta$ ($\nu$ = 1300–500 cm$^{-1}$).

| Pyro-420 | Pyro-750 | Pyro-870 | Pyro-$\beta$ | Assignment |
|---|---|---|---|---|
| **1237**[a], 1218 | 1258, **1241** | **1265**, **1248** | 1260, 1247 | A′[b] } $\nu_{as}$ $PO_3$ |
| | **1217** | **1218**, 1200 | 1218, 1205 | A′ } $\nu_{as}$ $PO_3$ |
| | 1184 | 1185 | 1184 | A′ } $\nu_{as}$ $PO_3$ |
| **1139** | **1141** | 1162, **1145**, 1130 | 1165, **1150**, **1132** | A′ } $\nu_{as}$ $PO_3$ |
| 1119 | 1117 | 1117 | 1115 | A′ + A″ } $\nu_{as}$ $PO_3$ |
| **1092** | **1088** | **1066** | 1087–1070, 1050 | A′ + A″ } $\nu_s$ $PO_3$ |
| | | 1008 | 1010 | A′ + A″ } $\nu_s$ $PO_3$ |
| **966** | **968** | **981** | 980 | $\nu$ V=O |
| | | **946**, 930, 921 | **940**, **927**, 922 | A′ + A″ $\nu_{as}$ P–O–P |
| **741** | **744** | **744** | **744** | A′ + A″ $\nu_s$ P–O–P |
| **631** | **633**, 624 | **635**, 622 | **638**, 621 | A′ + A″ } $\delta$ $PO_3$ |
| **578** | **577** | **564** | **562** | A′ } $\delta$ $PO_3$ |
| **513** | **513** | **515** | **515** | A′ } $\delta$ $PO_3$ |

[a] Bold numbers correspond to the most intense band(s) in the group.
[b] $C_s$ symmetry; after [1].

idence these polymorphs have failed. However, the known formation of polytypes [21] could be the reason why bands of Pyro-870 and Pyro-$\beta$ are shifted and/or split, so that the spectra look as blurred. Polytypes are likely to form during sintering of the materials and reduction of $\beta$-$VOPO_4$ [24]. Typically, bands at high wavenumber (>1240) and ca. 980–700 cm$^{-1}$ (here assigned to $\nu_{as}$ P–O–P) are found in polyphosphates. Whatever the explanation may be, it must be noted that the difference of particle morphology is accounted for by the difference of FTIR spectra, as already shown, e.g., in the cases of $TiO_2$ (rutile) or of ZnO [22,23].

### 3.3. TGA experiments

When comparing the TGA curves exhibited during their oxidation by Pyro-420 and Pyro-750 (figure 3(a)), it is seen that the onset of oxidation is the same (530 °C), but that the rate of oxidation of Pyro-420 is smaller than for Pyro-750. The gains of weight are smaller (4.2 and 4.9%) than the theoretical one (5.19 %), which is accounted for by the initial mean oxidation state of vanadium (4.15 and 4.01, respectively). $\gamma$-$VOPO_4$ [24] is the only oxidized phase detected by XRD after oxidation of Pyro-420 and Pyro-750.

The oxidation of Pyro-870 begins at lower temperature (480 °C) and ends at higher temperature (760 °C) than that of the other samples (figure 3(b)). The shape of the TGA curve is clearly different. Two oxidation steps are evidenced, the first at 480–530 °C and the second one at 530–760 °C. The final gain of weight is equal to the theoretical one, and the mean initial vanadium oxidation is assumed to be near 4.00. The exact value could not be obtained by titration because of the non-dissolution of Pyro-870 (table 1). The XRD pattern shows that a mixture of $\gamma$-$VOPO_4$ and $\beta$-$VOPO_4$ is recovered at the end of the experiment.

### 3.4. TAP experiments

The percentage of the oxygen uptake (called oxygen conversion) by each sample is plotted against the amount of oxygen pulsed in figure 4. The initial conversion begins near 90% for Pyro-420, and at 100% for Pyro-750 and Pyro-870, as expected from the initial amount of $V^{5+}$ in these solids (19, 5.6 and ∼0%, respectively). The oxygen conversion decreases rapidly and then more slowly when the number of pulses increases. The same amount of oxygen is stored during the experiment for all solids, but the rate is the highest in the case of Pyro-870. Examples of conversions are 15, 3 and near 0% for Pyro-420, Pyro-750 and Pyro-870, respectively, for $10^{19}$ $O_2$ molecules pulsed. Pyro-420 is the only sample which still stores oxygen when $20 \times 10^{18}$ $O_2$ are pulsed, since the conversion is close to 10%.

### 3.5. Catalytic properties

No deactivation of $(VO)_2P_2O_7$ was observed for the time of experiments (min. 48 h) at 420 °C under the air/butane flow. Selectivity to maleic anhydride and conversion of $n$-butane were obtained at the steady state, which was reached after a short stabilization period (0.5–1 h). The main by-products were CO, $CO_2$ and a very low amount of acetic acid was observed. After catalytic reaction, $(VO)_2P_2O_7$ was the only phase detected by XRD and no textural modification was revealed by XRD nor by TEM.

The best yield in maleic anhydride (9.6%) is obtained with Pyro-420 (table 3). Platy samples Pyro-420 and Pyro-750 have similar specific activity. The catalytic performance decreases when the temperature of calcination of the precursor increases, i.e., when the crystallinity of $(VO)_2P_2O_7$ increases. This trend has often been noticed by other groups [25,27]. The catalytic results (table 3) are clearly poorer than those generally given in literature [8,25]. The calcination of precursor under nitrogen atmosphere is known to minimize the formation of $V^{5+}$ species which are

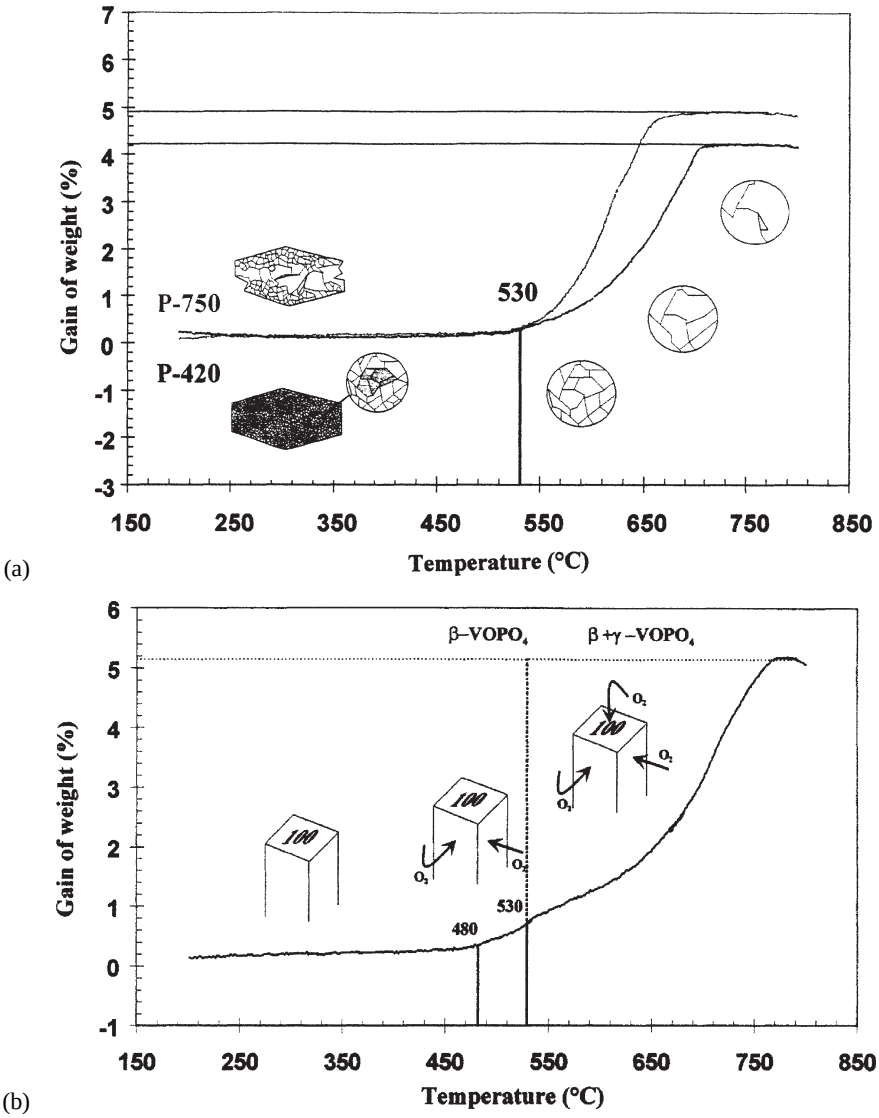


Figure 3. TGA of the oxidation of $(VO)_2P_2O_7$ samples. (a) Pyro-420 and Pyro-750 platelets (zooms show the rearrengement of the Pyro-420 nanostructure during heating). (b) Pyro-870 prisms (see text for details).

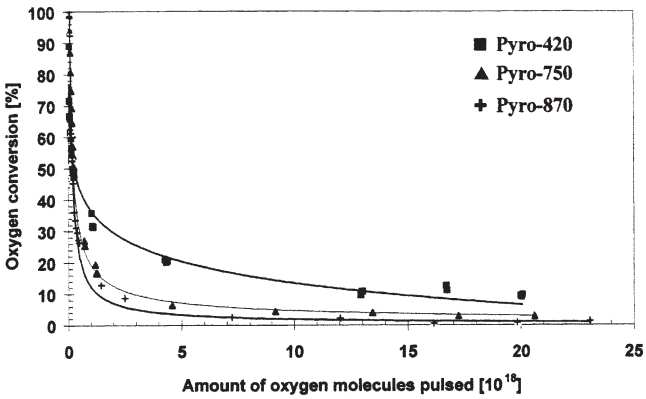


Figure 4. Oxygen uptake (conversion) vs. number of $^{16}O_2$ molecules pulsed over the $(VO)_2P_2O_7$ samples in a TAP reactor.

related to selectivity [27–31]. Moreover, the low surface area of each sample, which is inherited from that of the precursor [10], limits strongly the butane conversion.

Table 3
Catalytic performance of vanadyl pyrophosphate catalysts.

| Catalyst | $C$ (%) | $S_{MA}$ (%) | $S_{CO_x}$ (%) | $Y_{MA}$ (%) | Specific activity ($mol_{but}\ s^{-1}\ g^{-1} \times 10^7$) |
|---|---|---|---|---|---|
| Pyro-420 | 30.2 | 31.9 | 68.1 | 9.6 | 8 |
| Pyro-750 | 27.6 | 23.9 | 76.1 | 6.6 | 7.2 |
| Pyro-870 | 21.7 | 19.2 | 80.8 | 4.1 | 2.5 |

## 4. Discussion

TGA results (figure 3) show that the rate of oxidation of the most disordered solid, Pyro-420, is smaller than for Pyro-750, and that the temperature of beginning oxidation of the most ordered solid, Pyro-870, is the lowest. This trend seems surprising at first because, generally speaking, a disordered solid is more reactive. It means that the oxidation of vanadyl pyrophosphate depends strongly on the microstructure and on the morphology of the particles.

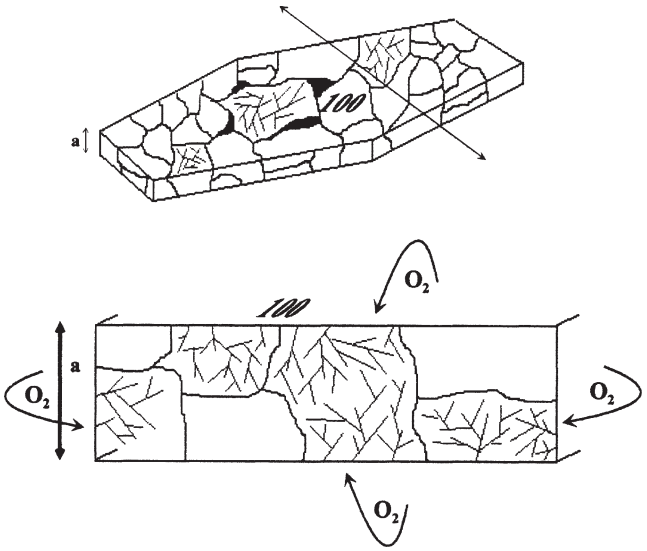


Figure 5. Model of the branching mechanism during the oxidation of a Pyro-750 particle (plate and side view).

The oxidation of Pyro-750 is schematized in figure 5. According to our recent findings [10], such particles are probably made up of one or two layers of crystallites in the [100] direction. We assume that the oxidation begins mainly on the $\{100\}$ faces of each crystallite and spreads inside the bulk by a classical branching mechanism [32]. No microstructural rearrangement or sintering process disturbs this oxidation mechanism, contrary to the case of Pyro-420. Indeed, according to the mosaic crystal model, the Pyro-420 particles are made up of several layers of crystallites in the [100] direction (figure 6). The oxidation process, which begins in our experimental conditions at 530 °C on the $\{100\}$ nanocrystallite faces, yields $\gamma$-$VOPO_4$. However, the reaction is slowed down because, at first, the propagation of the mechanism is stopped by defective zones, i.e., intercrystallite boundaries (figure 6). These zones being more reactive than the crystallites, are rapidly sursaturated with oxygen. The result is the formation of a diffusion barrier which hinders the oxidation of the bulk of crystallites. When the temperature is maintained at 530 °C, only a slight oxidation concerning the first layer of each Pyro-420 crystallite can be expected. When the temperature of reaction increases, the crystallinity of the material improves, owing to the usual mechanism of growth of coherent domains. The crystallite size increases and progressively the oxidation process expands inside the bulk of each crystallite, till the intercrystallite boundaries vanish. The rate-limiting step of this oxidation mechanism is then the rearrangement of the initial mosaic microstructure.

Older experiments performed in isothermal conditions [19,33] showed that $\gamma$-$VOPO_4$ was obtained by oxidation of a sample of $(VO)_2P_2O_7$, itself prepared by reduction in nitrogen of $\gamma$-$VOPO_4$ (or by dehydration of the precursor), and exhibiting the platy morphology. On the other hand, bulky crystals of $(VO)_2P_2O_7$ prepared by reduction of $\beta$-$VOPO_4$ were observed to give back $\beta$-$VOPO_4$ by oxidation. The composition of the final phase obtained during TGA is in accordance with these experiments since $\gamma$-$VOPO_4$ is recovered from Pyro-420 and Pyro-750, while, in the case of prismatic Pyro-870, a mixture of $\gamma$- and $\beta$-$VOPO_4$ is obtained. The presence of $\gamma$ and $\beta$ may account for the two steps of the TGA curve (figure 3(b)). According to the equilibrium shape of $(VO)_2P_2O_7$ [16], the area of $\{100\}$ faces would make 32% of the total external area, the remaining 68% corresponding to the perpendicular faces. In the case of Pyro-420 and Pyro-750, the $\{100\}$ faces are the most developed and they are oxidized to $\gamma$-$VOPO_4$. We assume that, for Pyro-870, the $\{100\}$ faces (32%) are oxidized to $\gamma$-$VOPO_4$, at the same onset temperature (530 °C) as for Pyro-420 and 750. The remaining 68% would be responsible for the formation of $\beta$-$VOPO_4$, which begins at lower temperature (480 °C). This is confirmed by the formation of $\beta$-$VOPO_4$ (beside remaining $(VO)_2P_2O_7$) when the experiment is stopped before reaching 530 °C. The energy of formation of $\gamma$-$VOPO_4$ is then probably higher than that of $\beta$-$VOPO_4$. Therefore, different polymorphs of $VOPO_4$ are obtained according to the crystal morphology exhibited by the particles, as schematized in figure 7.

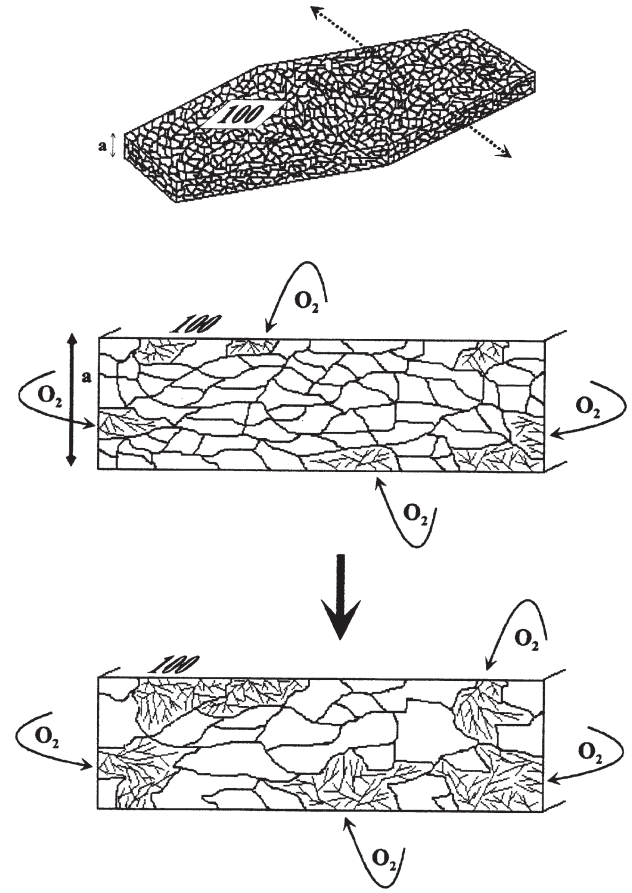


Figure 6. Model of the branching mechanism and of the structural rearrangement during the oxidation of a Pyro-420 particle (plate and side view).

TAP experiments (figure 4), which were conducted in isothermal conditions at low temperature (390 °C) to

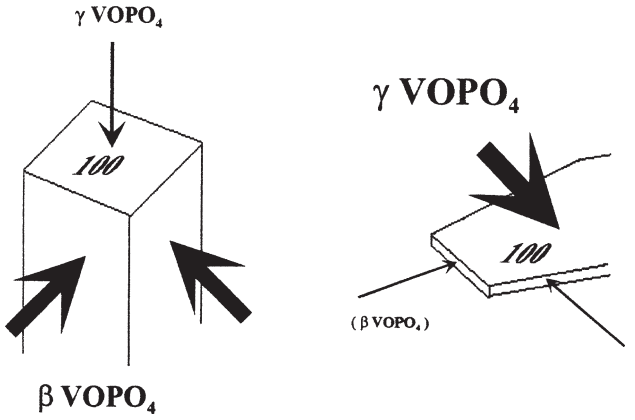


Figure 7. Model of the oxidation behavior of the two forms of $(VO)_2P_2O_7$. Large arrows indicate the prevailing mechanism: prisms yield mostly $\beta$-$VOPO_4$ (left) and plates yield mostly $\gamma$-$VOPO_4$ (right).

avoid any microstructural modification, but in vacuum ($10^{-4}$ atm), lead to similar interpretation. Because the platy particles of Pyro-420 are reoxidized slower than the prismatic particles of Pyro-870, the rate of oxidation is assumed to be higher when the oxidation proceeds parallel to the (100) planes than when it proceeds perpendicularly to them, as proposed in a former work [34]. Although particles of Pyro-750 are platy, their oxidation behavior is similar to that of Pyro-870. This apparent contradiction can be removed by considering the higher crystallinity, and also the larger amount of small faces perpendicular to $\{100\}$ due to the presence of voids and cracks in particles.

For each sample, the general trend of oxidation (figure 4) is normal. The $V^{4+}$ species are oxidized and the oxygen is incorporated into $(VO)_2P_2O_7$ according to the following redox reaction:

$$2V^{4+} + (1/2)O_2 \rightarrow 2V^{5+} + O^{2-}$$

The slowing-down of the curve with the amount of pulsed oxygen is related to the diffusion barrier which exists once the first layers of $(VO)_2P_2O_7$ have been oxidized. Pyro-420 behaves differently since the final value of oxygen conversion is 10% instead of 2% in the case of Pyro-750. Once more, the role of the microstructure in the oxidation process is highlighted: The intercrystallite boundaries are responsible for the storage of more oxygen in Pyro-420 than in the other particles which are in a more crystallized state and which even are monolithic, as for Pyro-870. The oxocapacity (defined here as the oxygen storage capacity) of $(VO)_2P_2O_7$ monocrystalline mosaic particles is then higher.

The latter remark is important if we consider, like Schuurman et al. [35], that the oxygens stored in the superficial lattice are active during the catalytic reaction, i.e., are directly inserted in the butane molecule. Consequently, the higher oxocapacity resulting from the mosaic microstructure is responsible for the better specific activity, i.e., the increase of the catalytic turnover, which is the case for the mosaic Pyro-420 catalyst (table 2). Conversely, the specific activity of the monolithic, highly crystalline, Pyro-870 material, is very low. A similar trend is followed by selectivity and yield in maleic anhydride since the highest values are obtained with Pyro-420. However, the interpretation deals with the crystalline faces which are preferentially exposed to butane molecules by the catalyst particles. Using the crystallographic model of active sites, Ziolkowski et al. [17,18,36] have shown that the $\{100\}$ face of $(VO)_2P_2O_7$ provides the number of oxygens and displays the active sites convenient for the direct and efficient oxidation of butane to maleic anhydride, while perpendicular faces do not. Zhang et al. [25] also suggested that the side faces of $(VO)_2P_2O_7$ along [100] do not possess the local structure which should orientate the reaction towards the formation of maleic anhydride. An unselective process was also evidenced by Okuhara et al. [37] who used single crystals of $(VO)_2P_2O_7$, the $\{100\}$ faces of which were poisoned with silica. As a consequence, a lower selectivity is exhibited by the prismatic catalyst, Pyro-870, because the $\{100\}$ face makes approximately one third of the total area [18]. Accordingly, the larger area of perpendicular faces facilitates the oxygen migration through the bulk, but also favors the total oxidation of $n$-butane to $CO_2$ which requires 13 instead of 7 catalyst $O^{2-}$ species in the case of the selective reaction. Finally, the slight increase in the number of perpendicular faces in Pyro-750 particles due to voids and cracks accounts for the slight decrease in selectivity compared with the (100) Pyro-420 platelets.

## 5. Conclusion

The three model samples are well differentiated by their characteristics: Pyro-420 has the highest amount of $V^{5+}$, the highest amount of $\{100\}$ facets as due to the mosaic microstructure, the highest capacity in oxygen. The highest yield of maleic anhydride is also obtained because of the highest conversion of $C_4$ and selectivity to MA. However, when compared to the best catalysts of literature, the performance is relatively poor. After the presence of $\{100\}$ faces, the other important feature to get high catalytic performance is the formation of $V^{5+}$ species which are needed to ensure the oxygen insertion in the hydrocarbon intermediate. First, the calcination of precursor in nitrogen is known to be not favorable. But it could be also that, in our samples, the $V^{5+}$ species are mostly present in the defect areas located between the $\{100\}$ mosaic facets, instead of being correctly displayed on the $\{100\}$ surface. Therefore, the present study, which completes the former one dealing with oxocapacity [38], illustrates once more the difficulty to fully understand the relative contribution of the various properties of $(VO)_2P_2O_7$.

## Acknowledgement

The authors thanks Dr. H.-W. Zanthoff (Lehrstuhl für Technische Chemie, Ruhr-Universität Bochum) for oxocapacity measurements performed with TAP equipment.

## References


[1] E. Bordes and P. Courtine, J. Catal. 57 (1979) 236.
[2] E. Bordes, in: *Elementary Reaction Steps in Heterogeneous Catalysis*, eds. R.W. Joyner and R.A. van Santen (Kluwer, Dordrecht, 1993) p. 137.
[3] B.G. Hyde and L.A. Bursill, in: *The Chemistry of Extended Defects in Nonmetallic Solids*, eds. L. Leroy-Eyring and M. O'Keeffe (North-Holland, Amsterdam, 1970) p. 347.
[4] P.L. Gai-Boyes, Catal. Rev. Sci. Eng. 34 (1992) 1.
[5] G.S. Rohrer, W. Lu, R.L. Smith and A. Hutchinson, Surf. Sci. 292 (1993) 261.
[6] R.L. Smith and G.S. Rohrer, J. Catal. 163 (1996) 12.
[7] P.L. Gai-Boyes, Acta Cryst. B 53 (1997) 346.
[8] G. Cavani and F. Trifirò, Catalysis 11 (1994) 246.
[9] E. Kesteman, M. Merzouki, B. Taouk, E. Bordes and R. Contractor, in: *Preparation of Catalysts VI*, Stud. Surf. Sci. Catal., Vol. 91, eds. G. Poncelet, J. Martens, B. Delmon, P.A. Jacobs and P. Grange (Elsevier, Amsterdam, 1995) p. 707.
[10] N. Duvauchelle, E. Kesteman, F. Oudet and E. Bordes, J. Solid State Chem. 137 (1998) 311.
[11] C.C. Torardi, Z.G. Li, H.S. Horowitz, W. Liang and M.H. Whangbo, J. Solid State Chem. 119 (1995) 349.
[12] P. Mars and D.W. van Krevelen, Chem. Eng. Sci. 3 (1954) 41.
[13] E. Bordes and R.M. Contractor, Topics Catal. 3 (1996) 365.
[14] G.K. Williamson and W.H. Hall, Acta Metall. 1 (1922) 22.
[15] N. Niwa and Y. Murakami, J. Catal. 76 (1982) 9.
[16] J.T. Gleaves, J.R. Ebner and T.C. Kuechler, Catal. Rev. Sci. Eng. 30 (1988) 49.
[17] J. Ziolkowski, Surf. Sci. 209 (1989) 536.
[18] J. Ziolkowski and E. Bordes, J. Mol. Catal. 84 (1993) 307.
[19] E. Bordes, P. Courtine and J.W. Johnson, J. Solid State Chem. 55 (1984) 270.
[20] E. Bordes, J.W. Johnson, A. Raminosona and P. Courtine, Mater. Sci. Monograf. B 28 (1985) 887.
[21] M.R. Thompson, A.C. Hess, J.B. Nicholas, J.C. White, J. Anchell and J.R. Ebner, in: *New Developments in Selective Oxidation II*, eds. V.C. Corberan and S.V. Bellon (Elsevier, Amsterdam, 1994) p. 167.
[22] M. Ocana, V. Fornés, J.V. Garcia Ramos and C.J. Serna, J. Solid State Chem. 75 (1988) 364.
[23] M. Andrés-Vergés, A. Mifsud and C.J. Serna, Mater. Lett. 8 (1989) 115.
[24] E. Bordes, Catal. Today 1 (1987) 499.
[25] R.M. Contractor, H.E. Bergna, H.S. Horowitz, C.M. Blackstone, U. Chowdhry and A.W. Sleight, Catalysis 1987 (1988) 645.
[26] Y. Zhang, R.P.A. Sneeden and J.C. Volta, Catal. Today 16 (1993) 39.
[27] K.E. Béré, Thesis, Université Lyon I, France (1996).
[28] G. Centi, F. Trifirò, J.R. Ebner and V.M. Franchetti, Chem. Rev. 88 (1988) 55.
[29] B.K. Hodnett, Catal. Today 1 (1987) 477.
[30] G. Centi, Catal. Today 16 (1993) 5.
[31] M.A. Pepera, J.L. Callahan, M.J. Desmond, E.C. Milberger, P.R. Blum and N.J. Bremer, J. Am. Chem. Soc. 107 (1985) 4883.
[32] B.A. Prout and F.C. Tompkins, Trans. Faraday Soc. 40 (1944) 488.
[33] E. Bordes and P. Courtine, J. Chem. Soc. Chem. Commun. (1985) 294.
[34] E. Bordes, Catal. Today 3 (1988) 163.
[35] Y. Schuurman, J.T. Gleaves, J.R. Ebner and M.J. Mummey, in: *New Developments in Selective Oxidation*, II World Congress & IV European Workshop Meeting, eds. V.C. Corberan and S.V. Bellon (1993) 40-1.
[36] J. Ziolkowski, E. Bordes and P. Courtine, J. Catal. 122 (1990) 126.
[37] T. Okuhara, K. Inumaru and M. Misono, in: *Symposium on Catalytic Selective Oxidation*, Am. Chem. Soc. Div. Petrol. Chem. (1992) p. 1222.
[38] N. Duvauchelle, H. Zanthoff, F. Hannour and E. Bordes, in: *$C_4$ Chemistry-Manufacture and Use of $C_4$ Hydrocarbons*, DGMK Conference, eds. W. Keim, B. Lücke and J. Weitkamp (1997) p. 181.